IMPACT OF MICROSTRUCTURAL PARAMETERS ON TOPOLOGY OPTIMIZATION OF STRUCTURES MADE OF COMPOSITES WITH ELLIPTICAL INCLUSIONS

BY

CHRISTOPHER KOZUCH

THESIS

Submitted in partial fulfillment of the requirements
for the degree of Master of Science in Theoretical and Applied Mechanics
in the Graduate College of the
University of Illinois at Urbana-Champaign, 2018

Urbana, Illinois

Adviser:

Professor Iwona Jasiuk

ABSTRACT

This thesis seeks to determine the relationship between the parameters that define microstructures composed of a matrix with periodic elliptical inclusions and the macroscopic shapes obtained using structural topology optimization. Stiffness properties for a range of microstructures were obtained computationally through homogenization, and these properties were used to conduct topology optimization on two canonical structural problems. Effectiveness was evaluated on the basis of final total strain energy when compared to a reference configuration. Local minima were found for the two structural problems and various microstructure configurations, indicating that the microstructure of composites with elliptical inclusions can be fine-tuned for topology optimization. For example, when making a cantilever beam from a material with soft, horizontal inclusions, ensuring that the aspect ratio of the inclusions is 2.25 will yield the best result after topology optimization is applied. Optimality criteria such as this have important implications in composite component design.

ACKNOWLEDGMENTS

I gratefully acknowledge partial funding from the National Science Foundation (NSF) I/UCRC grant (IIP-1362146).

TABLE OF CONTENTS

LIST OF FIGURES

CHAPTER 1

INTRODUCTION

Composites have long been an area of major interest, and there is widespread adoption in industry [1]. In addition to notable products such as the Boeing 787 Dreamliner and McLaren 570S, composites are being used in a wide range of aerospace, marine, energy, and infrastructure applications, to name a few [2–4]. They are often noted for their superior strength to weight ratios, corrosion resistance, and in some cases, high durability.

However, the term composites encompasses an enormous range of materials, from light carbon fiber polymer matrix composites to high strength metal matrix composites. This thesis focuses on composites that can be represented in two dimensions (2D) and contain elliptical inclusions. Ellipsoidal inclusions, which include elliptical inclusions as a limit case, have been widely used in material science and mechanics of materials, from Eshelby's seminal 1957 paper [5] and Hill's 1965 paper [6] to more recent applications with finite element analysis [7] and nanostructures [8]. This is due, in part, to the fact that ellipsoidal (or elliptical) inclusions can represent a wide array of composite materials, including particulate composites and fiber reinforced composites.

As such, composites that can be represented in this manner are found in a variety of fields. Bortot et al. investigated composites with ellipsoidal inclusions as soft electric circuits [9]. Wang demonstrated the relationship between elliptical fibers and the thermo-electric properties of a composite [10]. Saadat et al. showed how composites with ellipsoidal inclusions could be used to form attachments between tendon and bone [11]. Other applications include magnetics and heat transfer [12–14].

Because there is such a wide field of applications for these materials, designers are often confronted with the challenge of incorporating them into components. This has driven a need for advanced design tools. As a result, many product developers have turned to topology optimization [15]. Topol-

ogy optimization is a mathematical method for determining optimal surfaces or boundaries for given boundary conditions and optimization criteria. It can be used to optimize a number of physical aspects, including heat transfer, fluid flow, and acoustics, but topology optimization is most commonly used to develop products with optimal structural integrity [16].

Many of the common topology optimization methods have assumed homogeneous and isotropic material properties [16], and this is sufficient for many applications that use metals, polymers, or ceramics, but some have recognized that a more careful consideration of the microstructure is crucial to advanced design. Several methods have been developed to optimize not only the macrostructure of a component, but the microstructure as well [17, 18]. These approaches depend on inverse homogenization, which is a mathematical method for obtaining the microstructural design that most closely achieves a target stiffness [19].

While inverse homogenization can be extremely effective, it produces designs that are often impractical to implement at the desired length scale. For this reason, the following analysis will focus on the optimization of both the macrostructure and microstructure of a component, but with the additional constraint that the microstructure must be composed of elliptical inclusions. As stated above, such materials have a range of powerful applications. Additionally, recent improvements in advanced manufacturing techniques, specifically additive manufacturing, have allowed manufacturers to not only create complex macrostructures, but they are now able to also adjust some of the parameters that define the microstructure, such as the shape of the inclusions [20–23].

The overall objective of this thesis is to develop a novel understanding of the relationship between the parameters that define the microstructure of composites with elliptical inclusions and the resulting structural shapes obtained by topology optimization. It is hoped that this new approach will allow designers to apply topology optimization to such materials and structures in a more efficient and potent manner.

CHAPTER 2

PROBLEM DEFINITION

2.1 Microstructure

An evaluation of the impact of microstructural parameters must first begin with a definition of the microstructural model. Figure 2.1 shows the model and associated parameters. All analysis was confined to two dimensions using the plane stress assumption to increase computational efficiency. The ellipse was embedded in a unit cell matrix, and the geometry of the ellipse was defined by its semi-major axis, a, semi-minor axis, b, and the angle, θ, between the semi-major axis and the horizontal. Additionally, the volume fraction of the inclusion was set to 15% for all scenarios for better comparison between different trials. The value of 15% was chosen as a compromise between inclusion contribution and aspect ratio range because initial testing showed that lower values tended to reduce the contribution of the ellipse below the observable threshold and higher values caused inclusions with high aspect ratios to exceed the bounds of the unit cell.

A range of 25 angles and 25 aspect ratios were studied. The angles were equally spaced between 0 and π, and the aspect ratios were evenly distributed between 1 and 4.7255. The upper limit for the aspect ratios was chosen to prevent any interaction between the boundaries of the unit cell and the inclusion given the aforementioned volume fraction. The semi-major and semi-minor axis lengths were calculated from the aspect ratio and volume fraction using Equation (2.1) and Equation (2.2). Here, ζ is the aspect ratio (i.e. $\zeta = a/b$), and κ is the inclusion volume fraction.

$$a = \sqrt{\frac{\kappa\zeta}{\pi}} \tag{2.1}$$

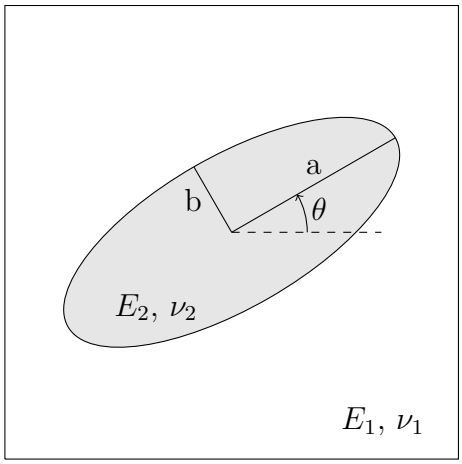

Figure 2.1: A unit cell model of a composite with a periodic arrangement of elliptical holes.

$$b = \sqrt{\frac{\kappa}{\pi\zeta}} \tag{2.2}$$

Both the inclusion and the matrix are assumed to be linear elastic, homogeneous, and isotropic. As such, the elastic properties of each are defined by their elastic modulus and Poisson's ratio. All further references to properties of the matrix will be marked with a subscript of 1 while properties of the inclusion will be marked with a subscript of 2. Two scenarios were considered. In the first, the inclusion is stiffer than the matrix by a factor of ten ($E_1/E_2 = 0.1$). In the second, the inclusion is softer than the matrix by a factor of ten ($E_1/E_2 = 10$). The Poisson's ratio was set to 0.33 for both materials in both scenarios.

2.2 Macrostructure

In addition to the microstructural model, the macro-scale boundary conditions used in the finite element analysis for the topology optimization must be defined. Two canonical topology optimization problems were chosen. The first, which is shown in Figure 2.2, is the Messerschmitt-Bolkow-Blohm (MBB) beam. This is composed of a rectangular domain that is pinned at both bottom corners and subjected to a vertical load at the center of the top edge [24]. Since the problem is symmetric, the domain size can be reduced by replacing the left half with rollers at the center, as shown in Figure 2.3.

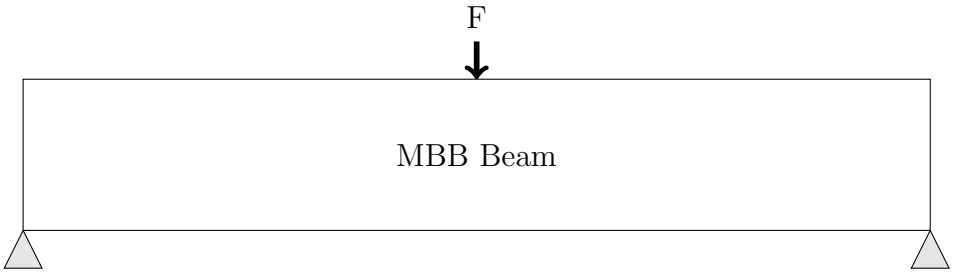

Figure 2.2: MBB beam boundary condition definition

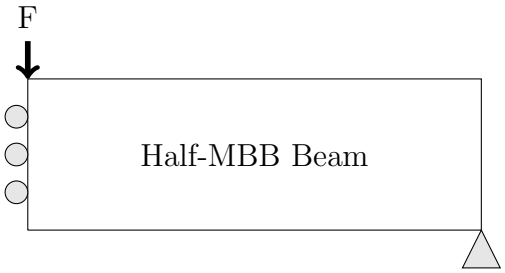

Figure 2.3: Half-MBB beam boundary condition definition

The second problem, which is shown in Figure 2.4, is a cantilever beam. This consists of rectangular domain which is fixed on the left and has a load on the center of the right. Both of these problems are used widely in the verification of topology optimization techniques [25–27].

Additionally, both cases have a horizontal length of 200 unit cells and a vertical height of 100 unit cells. Each cell will be represented by one element in the finite element model, and each one of those elements will have the stiffness that corresponds to the microstructure configuration. Finally, both the half-MBB beam and cantilever beam problems will be subject to a load with unity magnitude. Ultimately, the load magnitude is irrelevant since the topology optimization results will be insensitive to it. The reasons for this will become clear in Section 3.2.

Figure 2.4: Cantilever beam boundary condition definition

CHAPTER 3

METHODS

The analysis process is composed of three primary steps. First, homogenization is used to compute the effective stiffness tensor of the microstructural unit cell defined by a, b, θ, E_1, E_2, ν_1, and ν_2. As stated above, a finite element model with either half-MBB beam or cantilever beam boundary conditions is then created with each cell taking on the stiffness tensor produced in the previous step. Finally, topology optimization is carried out on the finite element model.

3.1 Homogenization

In order to perform homogenization, the microstructural model first has to be converted into a binary map. The domain is divided into a grid with 200 nodes along both axes. At each node point, the function for a rotated ellipse, which is shown in Equation (3.1), is evaluated. Nodes where V is found to be less than 1 are assigned a value of 2 to indicate that they lie inside the ellipse, and therefore represent the inclusion. All other nodes are assigned a value of 1 to indicate that they lie outside the ellipse, and therefore represent the matrix. The binary map and corresponding material properties are then input into the homogenization algorithm.

$$V = \left(\frac{x \cos\theta + y \sin\theta}{a} \right)^2 + \left(\frac{x \sin\theta - y \cos\theta}{b} \right)^2 \tag{3.1}$$

Methods for homogenization date back to the 1970s [28–30], and a multitude of approaches have been developed since then. The method known as asymptotic homogenization has emerged as an industry standard, especially for numerical applications [31–33]. This type of homogenization involves several assumptions: (i) the microstructure is periodic, (ii) the materials that

compose the microstructure are perfectly bonded, and (iii) there is a clear separation of length scales [34]. Often, there is criticism that accurate homogenization requires extreme separations of scale, but the technique has shown to be effective even when the length scales have reasonable separation [35]. Additionally, homogenization is often used in tandem with topology optimization [36–38].

The homogenization algorithm employed for the following analysis was adapted from [39], and a summary of the equations that were presented therein are provided below. The process is relatively straightforward. Prescribed strains, $\varepsilon_{pq}^{0(ij)}$, are applied under periodic boundary conditions and the resulting displacement fields, $u^{(kl)}$, are determined by solving Equation (3.2) via the finite element method. Here, C_{ijpq} denotes the local stiffness tensor, ϕ denotes the virtual displacement, and Equation (3.3) gives the strain definition.

$$\int_V C_{ijpq}\varepsilon_{ij}(\phi)\varepsilon_{pq}(u^{(kl)})dV = \int_V C_{ijpq}\varepsilon_{ij}(\phi)\varepsilon_{pq}^{0(kl)}dV \quad \forall\, \phi \in V \tag{3.2}$$

$$\varepsilon_{pq}^{(ij)} = \varepsilon_{pq}\left(u^{(ij)}\right) = \frac{1}{2}\left(u_{p,q}^{(ij)} + u_{q,p}^{(ij)}\right) \tag{3.3}$$

The homogenized stiffness tensor, C_{ijkl}^{H}, is then computed using Equation (3.4). For a 2D system using the assumptions listed in Chapter 2, this produces a `3x3` tensor.

$$C_{ijkl}^{H} = \frac{1}{|V|}\int_V C_{pqrs}\left(\varepsilon_{pq}^{0(ij)} - \varepsilon_{pq}^{(ij)}\right)\left(\varepsilon_{rs}^{0(kl)} - \varepsilon_{rs}^{(kl)}\right)dV \tag{3.4}$$

For the 2D case of plane stress, the local stiffness tensor, which we will now denote as $\mathbf{Q}$ to make the distinction between the 2D and 3D cases, can be computed from the Lamé constants using Equation (3.5). Here, λ is the first Lamé constant and μ is the second Lamé constant.

$$\mathbf{Q} = \lambda\begin{bmatrix}1 & 1 & 0\\ 1 & 1 & 0\\ 0 & 0 & 0\end{bmatrix} + \mu\begin{bmatrix}2 & 0 & 0\\ 0 & 2 & 0\\ 0 & 0 & 1\end{bmatrix} \tag{3.5}$$

Since the elastic properties were defined using the elastic modulus and Poisson's ratio, Equations (3.6) and (3.7) give the relationship between these

and the Lamé constants. Please note that for the plane stress case, the first Lamé constant must be modified as shown in Equation (3.8).

$$\lambda = \frac{\nu E}{(1+\nu)(1-2\nu)} \tag{3.6}$$

$$\mu = \frac{E}{2(1+\nu)} \tag{3.7}$$

$$\hat{\lambda} = \frac{2\mu\lambda}{\lambda + 2\mu} \tag{3.8}$$

All computations for the generation of the binary map and the execution of the homogenization method were carried out in MATLAB, as in [39].

3.1.1 Stiffness Tensor Rotation

While it is simple to compute the homogenized stiffness tensor for each value of θ, it is more computationally efficient to simply rotate the stiffness tensor obtained from the homogenization where $\theta = 0$ by the desired amount. Let $m = \cos\theta$ and $n = \sin\theta$. Then the rotated stiffness tensor is given by Equation (3.9).

$$\mathbf{Q}_{rot} = \begin{bmatrix} m^2 & n^2 & -2mn \\ n^2 & m^2 & 2mn \\ mn & -mn & m^2 - n^2 \end{bmatrix} \mathbf{Q} \begin{bmatrix} m^2 & n^2 & mn \\ n^2 & m^2 & -mn \\ -2mn & 2mn & m^2 - n^2 \end{bmatrix} \tag{3.9}$$

3.2 Topology Optimization

As stated in Chapter 1, topology optimization seeks the surface or boundary that minimizes a certain quantity, which is structural compliance in our case. Since compliance is the inverse of stiffness, this should produce a component with the maximum stiffness. A volume or mass target is also applied to the optimization process to bound the design space. There is a plethora of methods for achieving this, many of which are outlined in [40]. Most methods fall into one of three categories: (i) density based, (ii) discrete, and (iii) boundary variation.

Density based methods use the density at nodes or elements of a mesh as the design variables. Varying the density between 0 and 1 at these points serves to scale the physical properties at those points. The amount of variation is usually based on the sensitivity of the physical response of the design. Filters are also used to remove checker-boarding patterns that can arise [41]. The final design is usually extracted by placing an isosurface at a particular density value (often 0.5). While these methods are sometimes criticized for generating fuzzy design boundaries, they can be extremely efficient, both in implementation and resource use. The most common density based method is Solid Isotropic Material with Penalization (SIMP) [16].

In contrast, discrete methods (also known as hard kill methods) assign either 0 or 1 to the design variables to indicate void or material, respectively. However, like density based methods, checker-boarding can arise, so additional steps must be taken to combat this [42]. A key advantage of discrete methods is that they do not have fuzzy boundaries like density based methods, but they are heuristic formulations that do not guarantee an optimal design and can fail in some cases [43]. Common methods include Evolutionary Structural Optimization (ESO) and Bidirectional Evolutionary Structural Optimization (BESO). The primary difference between ESO and BESO is that ESO only removes material while BESO can both add and remove material [16].

Boundary variation methods are the most recent major addition to the topology optimization field. Instead of depending on a mesh of design variables like the previously discussed methods, boundary variation methods are based on implicit functions that define the boundary of the design. These methods are often confused with shape optimization, but they are distinct in the fact that they allow for the formation and destruction of voids. Boundary variation methods also have the advantage of producing well defined designs with crisp boundaries, but they can be resource intensive and highly dependent on the initial design guess [44]. The two most common boundary variation methods are the Level-Set Method and the Phase-Field Method [45, 46].

It is clear that there are advantages and disadvantages to each class of method. Since the following analysis will demand high computational resources, the resource efficiency of the SIMP method made it the most advantageous method for this application. Similar investigations have also used this method [37, 47]. To keep the implementation standardized and efficient, the

authors have adapted the highly optimized algorithm presented in [48], which assumes isotropic material, to handle anisotropic materials. The method and equations presented in [48] are summarized below.

Equation (3.10) shows the formal definition for the optimization problem using a meshed domain. For this application, $\mathbf{x}$ are the element density values, $\Psi(\mathbf{x})$ is the total compliance and f is the target volume fraction. $\mathbf{K}$, $\mathbf{U}$, and $\mathbf{F}$ are the stiffness matrix, displacement vector, and forcing vector, respectively.

$$\begin{aligned} \min_{\mathbf{x}} : \quad & \Psi(\mathbf{x}) = \mathbf{U}^T\mathbf{K}\mathbf{U} \\ \text{subject to} : \quad & V(\mathbf{x})/V_0 = f \\ & \mathbf{K}\mathbf{U} = \mathbf{F} \\ & \mathbf{0} \leq \mathbf{x} \leq \mathbf{1} \end{aligned} \tag{3.10}$$

As stated at the beginning of Chapter 3, the topology optimization method is applied to a finite element model where the boundary conditions are given by chosen loading problem and the stiffness of each element is described by the tensor produced by the homogenization process. In the SIMP method, an exponential penalization parameter, p, is used to produce a scaling factor, α_e, for each element based on the density of that element, as shown in Equation (3.12). Here, α_0 corresponds to a solid element, and is given a value of 1 while α_{min} corresponds to a void element, and is given a very small, but non-zero value to avoid singularities. For this application, α_{min} was set to 1×10^{-9} and p was set 3. This scaling factor is computed for each element and then used to update the overall stiffness matrix.

$$\hat{\mathbf{Q}}_e = \alpha(x_e)\mathbf{Q} \tag{3.11}$$

$$\alpha_e(x_e) = \alpha_{min} + x_e^p(\alpha_0 - \alpha_{min}) \tag{3.12}$$

Since the density, x_e, is also the design variable, it requires an update scheme. The update scheme uses a simple move limiter, m, and numerical damper, η, as shown in Equation (3.13), but is effectively a function of the sensitivity. The sensitivity is computed using Equation (3.14), where ξ is the Lagrange multiplier used to enforce the volume fraction requirement from

Equation (3.10). For this application, m was chosen to be 0.2 and η was set to 0.5, as suggested by [48].

$$x_e^{new} = \begin{cases} \max(0,\, x_e - m), & x_e B_e^{\eta} \leq \max(0,\, x_e - m) \\ \min(1,\, x_e + m), & x_e B_e^{\eta} \geq \min(1,\, x_e + m) \\ x_e B_e^{\eta}, & \text{otherwise} \end{cases} \tag{3.13}$$

$$B_e = \frac{-\partial \Psi / \partial x_e}{\xi(\partial V / \partial x_e)} \tag{3.14}$$

$$\partial \Psi / \partial x_e = -p x_e^{(p-1)} (\alpha_0 - \alpha_{min}) \mathbf{U}_e^T \mathbf{K}_e \mathbf{U}_e \tag{3.15}$$

$$\partial V / \partial x_e = 1 \tag{3.16}$$

To avoid checker-boarding, sensitivity based filtering is also performed on each element using Equation (3.17) and Equation (3.18). Here, γ is a small number to prevent division by zero, $\Delta(e,\, i)$ is the center-to-center distance between elements e and i, N_e is the set of all elements for which H_{ei} is positive, and r_{min} is the filter radius. The filter radius controls how much smoothing takes place. A high filter radius will ensure a smooth result, but may remove small features from the design while the converse is true for a low filter radius. It is relatively standard to set the filter radius to 1.5 times the element size, which is what was done here. Following [48], γ was set to 1×10^{-3}.

$$\widehat{\frac{\partial \Psi}{\partial x_e}} = \left[\max(\gamma, x_e) \sum_{i \in N_e} H_{ei} \right]^{-1} \sum_{i \in N_e} H_{ei} x_i \frac{\partial \Psi}{\partial x_i} \tag{3.17}$$

$$H_{ei} = r_{min} - \Delta(e,\, i) \tag{3.18}$$

This whole process is iterated over until one of the following two conditions is met: (i) the cumulative change in successive designs that satisfy the optimization conditions falls below a threshold or (ii) a maximum number of iterations is reached. Normally, if the latter condition is met, the process is considered to have failed. As with [48], all computations for the topology optimization were carried out in MATLAB.

CHAPTER 4

RESULTS AND DISCUSSION

The overall topology optimization computational process is very efficient. One execution of the combined inclusion generation, homogenization, and topology optimization process takes about 100 seconds on a standard desktop computer with a 3.20 GHz processor and 8 GB of RAM. The set of combined process executions for the different microstructure and boundary condition parameters described in Chapter 2 were run in parallel using the built-in MATLAB function `parfor`.

Given the focus on design, the results have been split into two sections. The first identifies interesting qualitative results concerning specific features of the resultant designs, while the second provides detailed quantitative analysis.

4.1 Qualitative Analysis

Figure 4.1 shows the resulting binary maps generated for an example set of stiff inclusions and their corresponding homogenized stiffness tensors. As expected, the circular inclusion in Figure 4.1a produces a nearly isotropic tensor (shown in Figure 4.1b) because the inclusion is uniform in all 2D orientations and has relatively low volume fraction. The tensor is orthotropic, and not isotropic, because the unit cell is square [49,50]. Figure 4.1c increases the aspect ratio to 3, which destroys the near isotropy, as evidenced by the inequality between elements Q_{11} and Q_{22} in Figure 4.1d. However, the symmetry about the central horizontal and vertical axes can still be seen in the fact that $Q_{13} = Q_{23} = 0$. Finally, Figure 4.1e simply rotates the map seen in Figure 4.1c by $\pi/4$. Again, we see the expected result where $Q_{11} = Q_{22}$ and $Q_{13} = Q_{23} \neq 0$ in Figure 4.1f.

Figure 4.2 shows the optimized topology for the half-MBB problem when the microstructure is composed of stiff, thin inclusions. The position of each

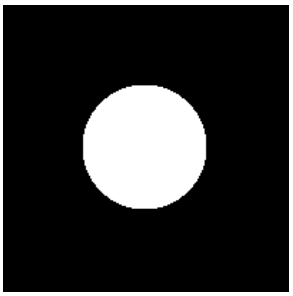

(a) Binary map for $a/b = 1$

$$\begin{bmatrix} 1.3778 & 0.4426 & 0.0000 \\ 0.4426 & 1.3778 & 0.0000 \\ 0.0000 & 0.0000 & 0.4510 \end{bmatrix}$$

(b) Stiffness tensor for $a/b = 1$

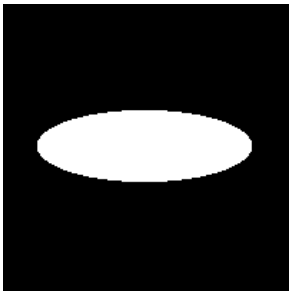

(c) Binary map for $a/b = 3$, $\theta = 0$

$$\begin{bmatrix} 1.5882 & 0.4395 & 0.0000 \\ 0.4395 & 1.3160 & 0.0000 \\ 0.0000 & 0.0000 & 0.4432 \end{bmatrix}$$

(d) Stiffness tensor for $a/b = 3$, $\theta = 0$

(e) Binary map for $a/b = 3$, $\theta = \pi/4$

$$\begin{bmatrix} 1.3869 & 0.4773 & 0.0459 \\ 0.4773 & 1.3869 & 0.0459 \\ 0.0459 & 0.0459 & 0.4751 \end{bmatrix}$$

(f) Stiffness tensor for $a/b = 3$, $\theta = \pi/4$

Figure 4.1: Stiffness tensor results of the homogenization process for stiff inclusions

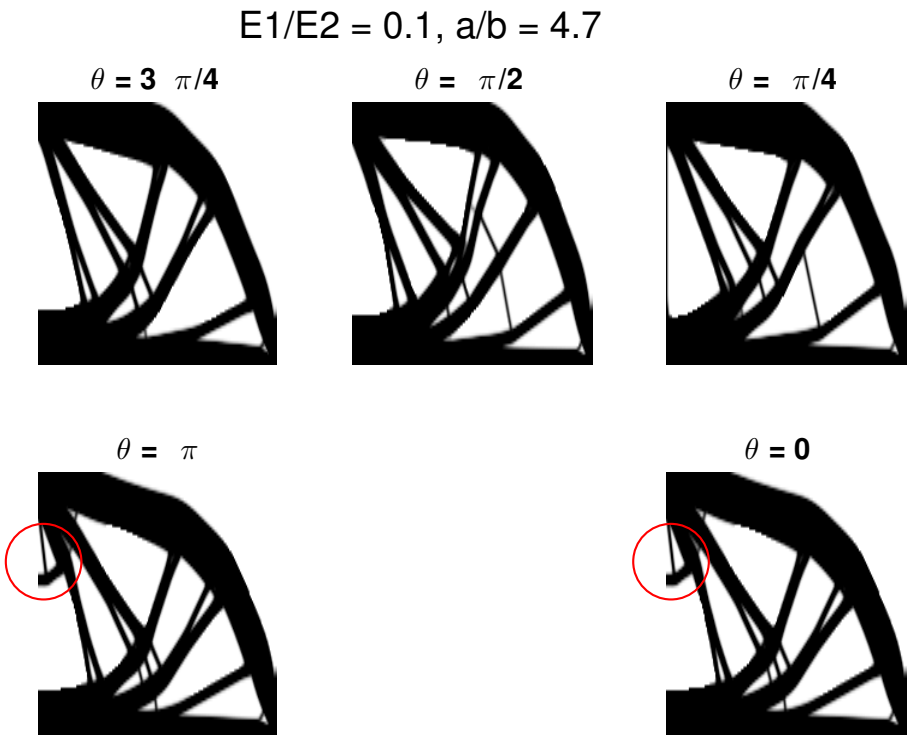

Figure 4.2: Design results for half-MBB problem

image is arranged to correspond with the angle of the inclusion. As expected, the designs for $\theta = 0$ and $\theta = \pi$ are identical since they produce identical inclusion orientations. However, there are clear differences with the other designs. None of the other designs exhibit the horizontal segment in the upper left corner (marked by the red circles), but they do form progressively longer connections with upper edge of the domain as you move from left to right. This forces the designs in the upper row to have a much steeper right side than those found in the lower row. A similar effect can be seen in the results obtained by [51].

Figure 4.3 shows the results for the same microstructures used in Figure 4.2, but for the cantilever problem. Again, we see that the designs for $\theta = 0$ and $\theta = \pi$ are identical. What is more interesting is that while all of the designs share the same basic elements, there are a few points of interest that move in direct response to the angle of the inclusions. As the dashed red line indicates, the intersection of the `X` feature on the left of the designs is perfectly centered for $\theta = \pi/2$. However, it is higher for the $\theta = \pi/4$ design and lower for the $\theta = 3\pi/4$ design. In fact, the design for $\theta = 3\pi/4$ is exactly equal to design for $\theta = \pi/4$ if it were reflected about the horizontal center

line. While one might attribute this simply to the fact that the microstructure for $\theta = 3\pi/4$ is a reflection about the horizontal of the microstructure for $\theta = \pi/4$, it is important to note that we do not see this result for the half-MBB problem. It is therefore the confluence of the horizontal symmetry in both the microstructure and the macrostructure that produces the symmetry in the final design.

4.2 Quantitative Analysis

Four types of problem spaces were investigated. These are each shown in Figure 4.4. The top row shows results for the cantilever problem and the bottom row shows results for the half-MBB problem. Additionally, the left column corresponds to soft inclusions while the right column corresponds to stiff inclusions. Since the total strain energy (compliance) was the minimization function, it was used as the basis for comparison. Therefore, smaller resultant values indicate more effective designs. It is also important to note that all results presented in Figure 4.4 have been normalized against the result obtained with an inclusion aspect ratio of 1 for the relevant problem space.

There are a few points of note concerning the surface plots. Probably the most obvious is that the results obtained with soft inclusions are the inverse of those obtained with stiff inclusions in several respects. While the most effective aspect ratio for the soft inclusions appears to be 1, the stiff inclusions minimize strain energy best at high aspect ratios (if the orientation is horizontal). Additionally, the soft inclusions display relatively constant strain energy at horizontal orientations while the stiff inclusions do the same at vertical orientations. Similar results were observed through experimentation for toughness [52]. Conversely, the disparities between the two boundary condition scenarios are quite small. The most noticeable difference is that Figure 4.4c has a small lip in the back corner that is not seen in Figure 4.4a.

Since it is difficult to interpret some relationships from surface plots, several line plots have been extracted. Figure 4.5 shows the normalized strain energy response to rotation angle when the aspect ratio is held at 3. In this case, the normalizing scenario is that of an inclusion with horizontal orientation and an aspect ratio of 3. There are three key points of interest in these

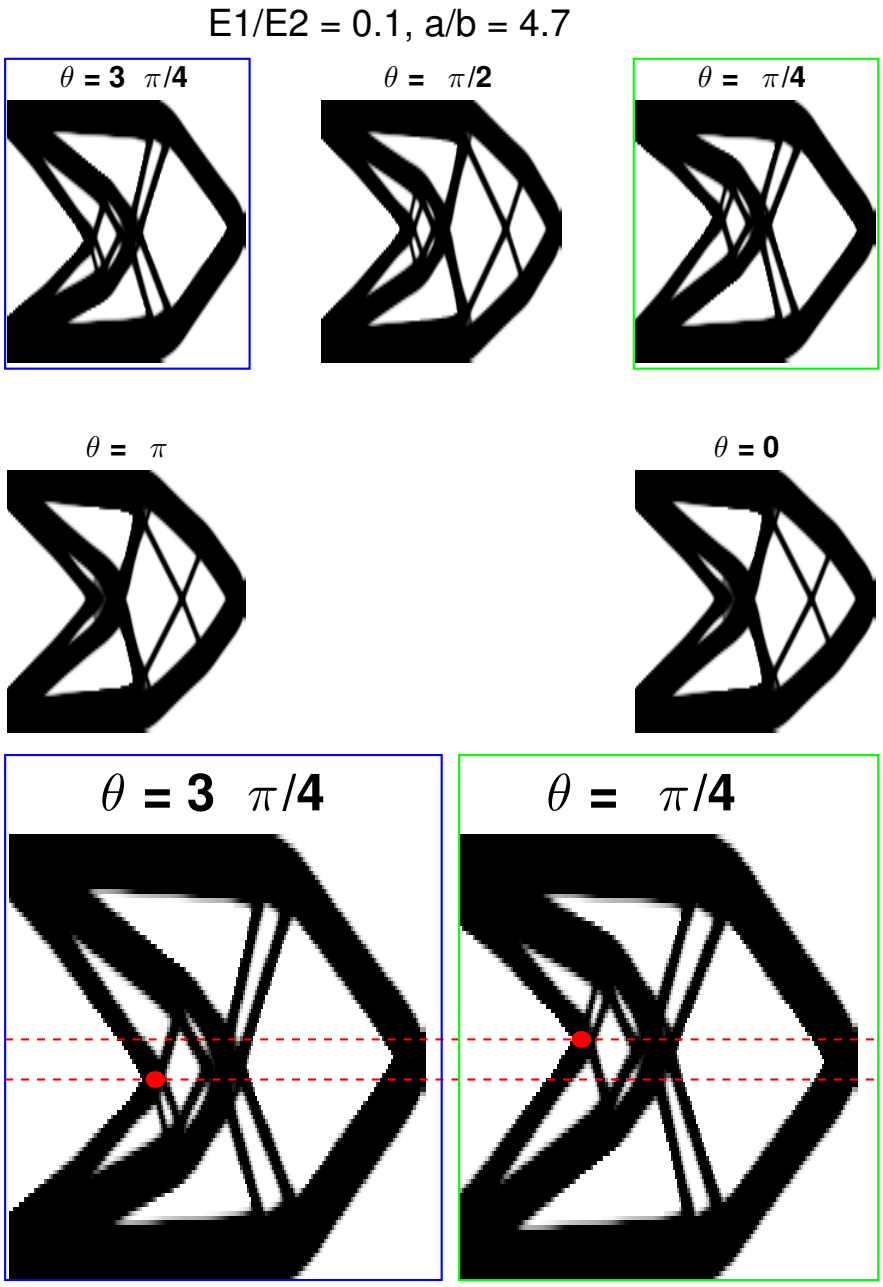

Figure 4.3: Design results for cantilever problem

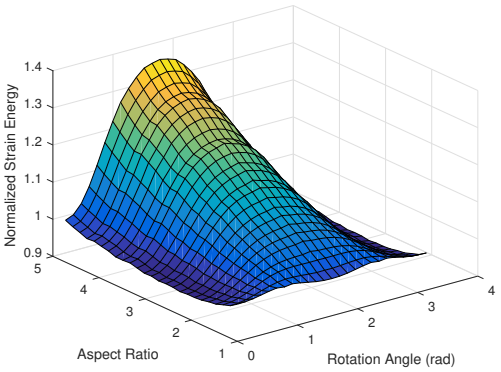

(a) cantilever problem with soft inclusions

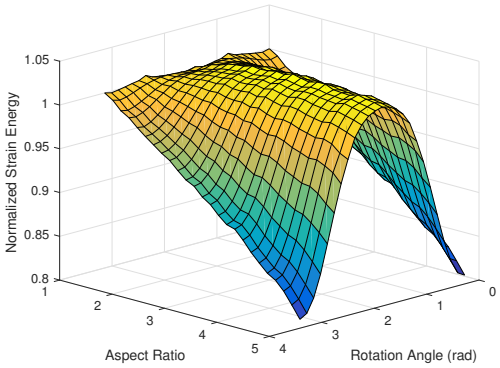

(b) cantilever problem with stiff inclusions

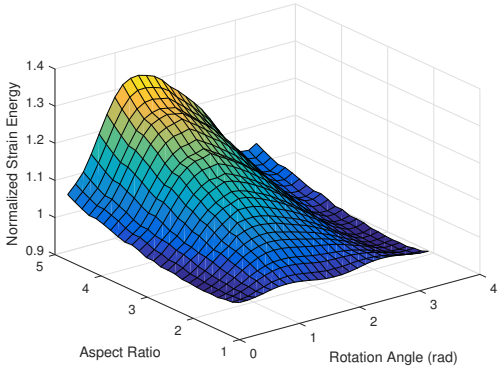

(c) half-MBB problem with soft inclusions

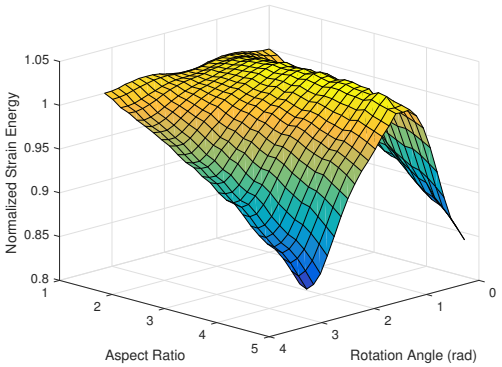

(d) half-MBB problem with stiff inclusions

Figure 4.4: Normalized strain energy vs. aspect ratio and rotation angle (note that the plots have been rotated for the best viewing angle)

plots. First, the cantilever problem demonstrates a clear symmetry about $\theta = \pi/2$ while the half-MBB problem is skewed to the left (which explains the small lip noted in the previous paragraph). Second, the half-MBB problem has a local minimum just shy of $\theta = \pi$ while the cantilever problem has no local minima. Points one and two are both most likely due to the vertical symmetry of the half-MBB problem. Since the rollers were placed on the left and the load placed on top, inclusions that align between the top left and the bottom right form a triangular support structure when they are reflected across the left edge of the domain. This triangle formation can be observed in some examples presented in [15]. Third, the range of normalized strain energies achieved by the soft inclusion scenario is almost twice that of the stiff inclusions. This is to be expected since the rotation of a stiff inclusion will contribute more than that of a soft inclusion where a majority of the load is carried by the matrix.

Figure 4.6 performs the same function as Figure 4.5, except it varies aspect ratio instead of orientation angle. As with the surface plots, the results have been normalized against an aspect ratio of 1. It is immediately apparent that these plots do not share the same smoothness shown in Figure 4.5, but important trends can still be observed. A key feature of all four plots is that the overall trends seem to be almost entirely independent of the macrostructure problems, which is in direct contrast with the relationship between normalized strain energy and rotation angle discussed above.

It is also interesting to note that stiff, vertical inclusions and soft, horizontal inclusions behave in the same, but inverse, manner. This can most likely be explained by the fact that both macrostructure problems have vertical loading. Therefore, microstructures that have strong vertical support will behave in a similar manner. In the case of a stiff, vertical inclusions, it is clear that there will be strong vertical support. However, in the case of soft horizontal inclusions, it is the absence of the soft inclusion along the vertical axis (and therefore the presence of stiff matrix) that gives the microstructure vertical strength. The opposite can be seen in the fact that stiff, horizontal inclusions behave in the same, but inverse, manner as soft, vertical inclusions.

Additionally, from an optimization viewpoint, the local minima and maxima shown in Figure 4.6c and Figure 4.6b, respectively, are even more interesting. While the microstructures with poor vertical support display nearly linear relationships, those with strong vertical support are parabolic. This

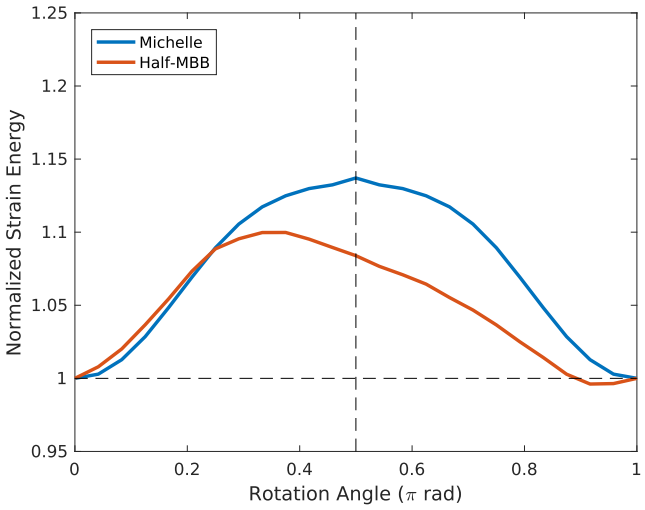

(a) Stiff inclusion, $a/b = 3$

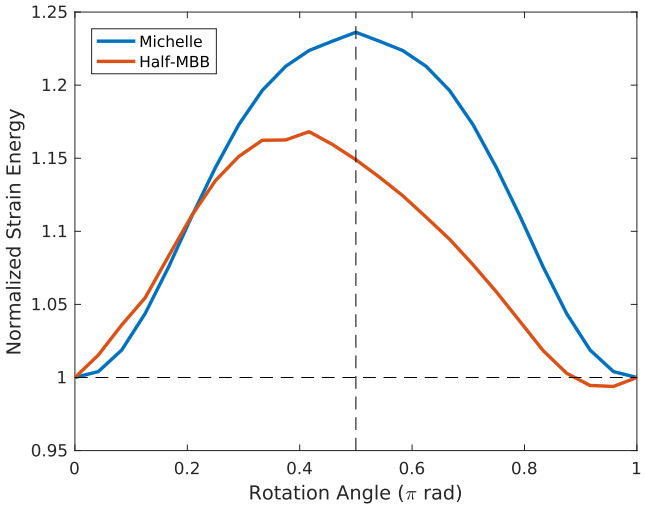

(b) Soft inclusion, $a/b = 3$

Figure 4.5: Normalized strain energy vs. angle

leads to the conclusion that, for soft, horizontal inclusions, there exists a "golden aspect ratio" at about 1.5 for the half-MBB problem and around 2.25 for the cantilever problem. The existence of such values could be extremely useful for designers who need to embed soft inclusions for any range of reasons but would also like to maintain good stiffness. Conversely, designers who must embed stiff, vertical inclusions must avoid similar values.

The final points that needs to be made for these plots concerns Figure 4.6a. It shows that higher aspect ratios for stiff, horizontal inclusions increases the effectiveness of the design. This contradicts most engineering practices which seek to minimize the stress concentrations formed by inclusions with high aspect ratios [53, 54]. There are two reasons for this. First is that all analysis conducted here assumed an entirely elastic response without any fracture. Second, both macrostructure problems are beam problems with vertical loads, so extremely flat inclusions prevent bending when the matrix is soft. Future work should repeat the executed process with penalties for material failure, as described in [55], to determine if this result is more general.

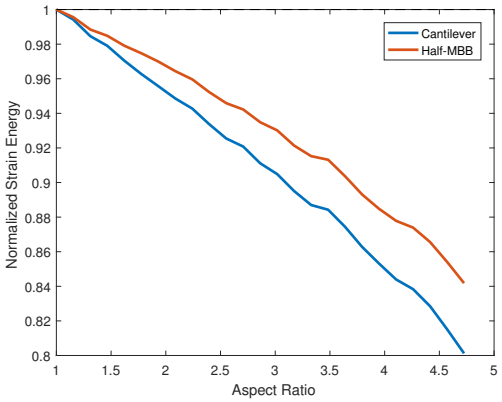

(a) Stiff, horizontal inclusions

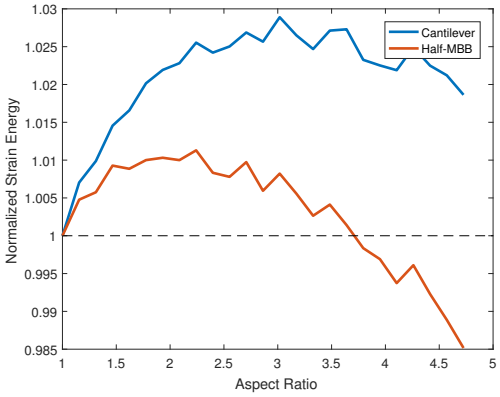

(b) Stiff, vertical inclusions

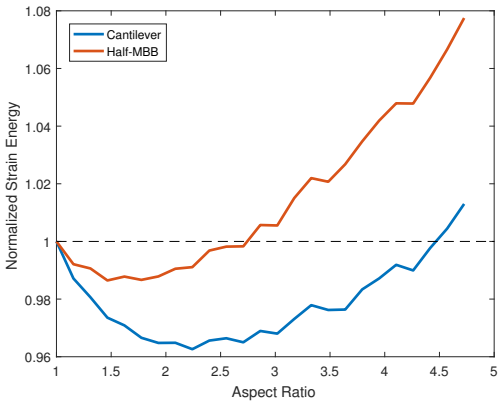

(c) Soft, horizontal inclusions

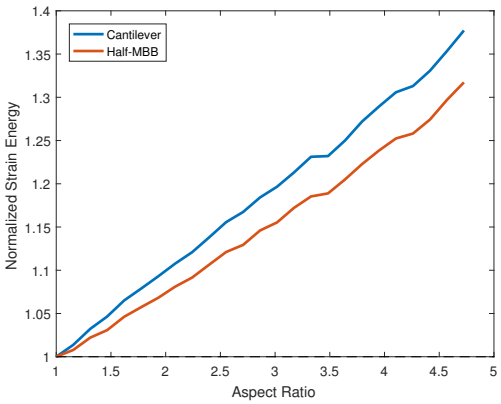

(d) Soft, vertical inclusions

Figure 4.6: Normalized strain energy vs. aspect ratio

CHAPTER 5

CONCLUSIONS

Chapter 4 demonstrates that the various microstructure and macrostructure design parameters described in Chapter 2 have a large impact on the effectiveness of topology optimization when applied to composites with elliptical inclusions. The following is a short list of how some of the most critical parameters interact with optimization process.

- Clearly discernible design feature move in direct relation to changes in the microstructure.
- Interactions between both the microstructure and macrostructure configurations dictate the symmetry and presence of local minima when comparing effectiveness and the microstructure orientation (the stiffness ratio plays a minimal role).
- The optimization effectiveness is a smooth function of the orientation angle, but not the aspect ratio.
- The stiffness ratio plays a major role in determining the relationship between the effectiveness and the aspect ratio.
- There exist "golden aspect ratios" for some microstructures that are local minima of the normalized strain energy.

CHAPTER 6

EXTENSION AND FUTURE WORK

Up to this point, every design that has been presented was composed of homogenized material with one type of microstructure.. However, one is not restricted to this case. By modifying the methods presented above, it is possible to select the optimal microstructure on an element-by-element basis. An example of this is presented in Section 6.1.

6.1 Extension to Optimization of Inclusion Volume Fraction

For all of the previous analysis, the volume fraction of the inclusion was held at 15%, as discussed in Section 2.1. Now, consider the case where the design variable is the inclusion volume fraction, κ, instead of the density. This means that the element stiffness can no longer be simply scaled using Equation (3.12). Instead, homogenization is used to compute the material stiffness for a range of inclusion volume fractions. (For simplicity, the aspect ratio was held at unity.) Since the trends for each stiffness component are simple and smooth, as shown in Figure 6.1, the relationships can be fit with polynomial curves, f_i. Using symmetry, the material stiffness tensor can therefore be expressed using Equation (6.1). Now the scaling function presented in Equation (3.12) can be replace with Equation (6.2).

$$\mathbf{Q}(\kappa) = \begin{bmatrix} f_1(\kappa) & f_6(\kappa) & f_5(\kappa) \\ f_6(\kappa) & f_2(\kappa) & f_4(\kappa) \\ f_5(\kappa) & f_4(\kappa) & f_3(\kappa) \end{bmatrix} \tag{6.1}$$

$$\hat{\mathbf{Q}}(\kappa) = \begin{bmatrix} f_1(\kappa^p) & f_6(\kappa^p) & f_5(\kappa^p) \\ f_6(\kappa^p) & f_2(\kappa^p) & f_4(\kappa^p) \\ f_5(\kappa^p) & f_4(\kappa^p) & f_3(\kappa^p) \end{bmatrix} \tag{6.2}$$

Additionally, the partial derivative shown in Equation (3.15) must be modified. Since the expression containing the design variable can no longer be pulled outside the element compliance term, the equation must be rewritten as shown in Equation (6.3). The partial derivative of the element stiffness matrix with respect to the inclusion volume fraction is obtained by building the element stiffness matrix in the normal manner, with the exception that the material stiffness tensor is replaced with $\hat{\mathbf{Q}}'$, which is given in Equation (6.4). Here, f_i' denotes the derivative of f_i with respect to κ.

$$\partial\Psi/\partial x_e = \mathbf{U}_e^T \frac{\partial \mathbf{K}_e}{\partial \kappa} \mathbf{U}_e \tag{6.3}$$

$$\hat{\mathbf{Q}}'(\kappa) = -p\kappa^{(p-1)} \begin{bmatrix} f_1'(\kappa^p) & f_6'(\kappa^p) & f_5'(\kappa^p) \\ f_6'(\kappa^p) & f_2'(\kappa^p) & f_4'(\kappa^p) \\ f_5'(\kappa^p) & f_4'(\kappa^p) & f_3'(\kappa^p) \end{bmatrix} \tag{6.4}$$

Finally, it is useful to note that the filtering discussed in Section 3.2 is no longer required. This is because the solution now marks the size of the inclusion in each element, not the presence of material or void, so sharp discontinuities are not an issue.

Figure 6.2 shows the result of applying the adjustments discussed above to the MBB-beam problem defined in Section 2.2. The black region denotes elements with a maximum sized inclusion while the white region denotes elements with no inclusion (i.e., composed entirely of matrix). The fact that the lower bound is matrix and not void allows the black regions to be disconnected. The jagged edges are a result of removing the filter.

It is interesting to note, as evidence by the absence of any gray in the figure, that even with the filter removed, each element takes on one of the extremes: either entirely matrix or maximum sized inclusion. This demonstrates that a maximally stiff element is much more valuable to the overall stiffness than an element with intermediate stiffness.

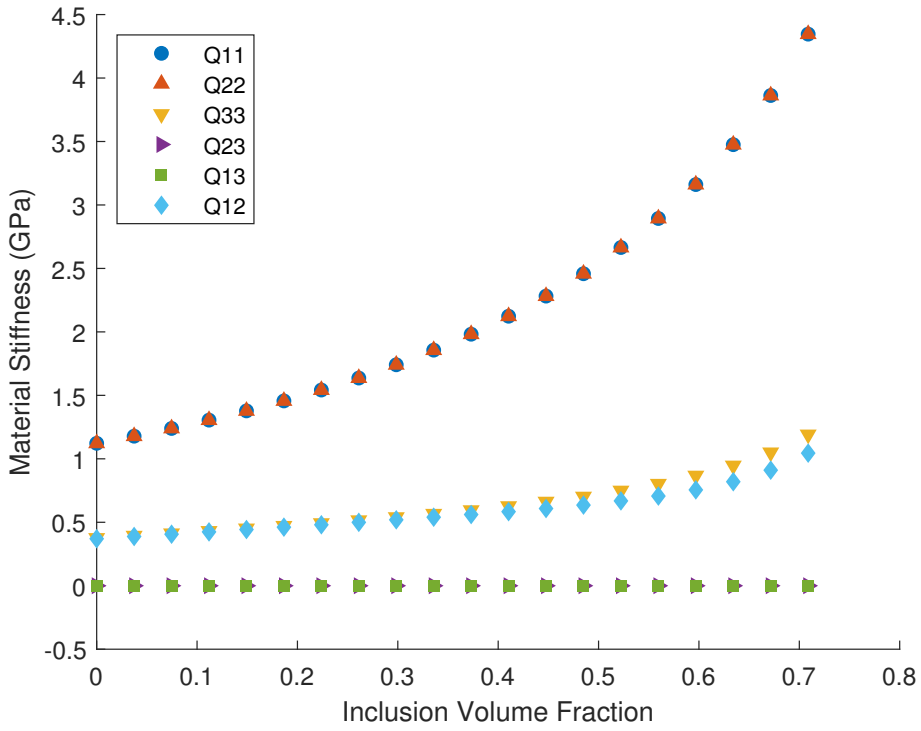

Figure 6.1: Relationship between inclusion volume fraction and material stiffness

Figure 6.2: Result of microstructural optimization

6.2 Future Work

There are several directions in which to take this work. As mentioned in Chapter 3, one obvious area of future application would be to extend the current work to outside linear elasticity. While many engineering metals can be accurately described by linear elasticity, materials commonly found in composites, such as polymers, require more advanced material models. Althought such an implementation will require significantly more computational resources, it could provide more accurate insight. Another logical extension of this work would be analysis in three dimensions. While 2D analysis can provide useful information on trends and certain classes of problems, it is impossible to obtain the full picture without also analyzing 3D cases.

Finally, an additional direction for future work could be an extension of the process described in Section 6.1 to other microstructural variables, such as rotation angle and aspect ratio. These pose significant challenges with uniqueness as the volume fraction requirement outlined in Equation (3.10) would no longer apply, but such a capability might have powerful implications. There also remains the possibility of optimizing more than one microstructural parameter at the same time.

REFERENCES

[1] B. Agarwal, *Analysis and performance of fiber composites*. Hoboken, NJ: Wiley, 2018.

[2] S. Tang and C. Hu, "Design, preparation and properties of carbon fiber reinforced ultra-high temperature ceramic composites for aerospace applications: A review," *J. of Materials Sci. & Technology*, vol. 33, no. 2, pp. 117 – 130, 2017.

[3] P. Davies and Y. D. Rajapakse, *Durability of composites in a marine environment*. Amsterdam: Springer, 2016.

[4] B. Noton, *Engineering applications of composites*. New York: Academic Press, 1974.

[5] J. D. Eshelby, "The determination of the elastic field of an ellipsoidal inclusion, and related problems," *Proceedings of the Royal Society of London A: Mathematical, Physical and Engineering Sci.s*, vol. 241, no. 1226, pp. 376–396, 1957.

[6] R. Hill, "A self-consistent mechanics of composite materials," *J. of the Mechanics and Phys. of Solids*, vol. 13, no. 4, pp. 213 – 222, 1965.

[7] S. Ghosh and S. Moorthy, "Three dimensional voronoi cell finite element model for microstructures with ellipsoidal heterogeneties," *Computational Mechanics*, vol. 34, no. 6, pp. 510–531, Nov 2004.

[8] P. Sharma and S. Ganti, "Size-dependent eshelbys tensor for embedded nano-inclusions incorporating surface/interface energies," *J. of Applied Mechanics*, vol. 71, no. 5, pp. 663–671, 2004.

[9] E. Bortot, R. Denzer, A. Menzel, and M. Gei, "Analysis of viscoelastic soft dielectric elastomer generators operating in an electrical circuit," *International J. of Solids and Structures*, vol. 78, pp. 205–215, 2016.

[10] Y.-Z. Wang, "Effective material properties of thermoelectric composites with elliptical fibers," *Applied Phys. A*, vol. 119, no. 3, pp. 1081–1085, 2015.

[11] F. Saadat, V. Birman, S. Thomopoulos, and G. M. Genin, "Effective elastic properties of a composite containing multiple types of anisotropic ellipsoidal inclusions, with application to the attachment of tendon to bone," *J. of the Mechanics and Phys. of Solids*, vol. 82, pp. 367–377, 2015.

[12] A. Goshkoderia and S. Rudykh, "Stability of magnetoactive composites with periodic microstructures undergoing finite strains in the presence of a magnetic field," *Composites Part B: Engineering*, vol. 128, pp. 19–29, 2017.

[13] N. Bonfoh, C. Dreistadt, and H. Sabar, "Micromechanical modeling of the anisotropic thermal conductivity of ellipsoidal inclusion-reinforced composite materials with weakly conducting interfaces," *International J. of Heat and Mass Transfer*, vol. 108, pp. 1727–1739, 2017.

[14] W. Kaddouri, A. El Moumen, T. Kanit, S. Madani, and A. Imad, "On the effect of inclusion shape on effective thermal conductivity of heterogeneous materials," *Mechanics of Materials*, vol. 92, pp. 28–41, 2016.

[15] J.-H. Zhu, W.-H. Zhang, and L. Xia, "Topology optimization in aircraft and aerospace structures design," *Archives of Computational Methods in Engineering*, vol. 23, no. 4, pp. 595–622, Dec 2016.

[16] J. D. Deaton and R. V. Grandhi, "A survey of structural and multidisciplinary continuum topology optimization: post 2000," *Structural and Multidisciplinary Optimization*, vol. 49, no. 1, pp. 1–38, 2014.

[17] L. Xia and P. Breitkopf, "Concurrent topology optimization design of material and structure within FE2 nonlinear multiscale analysis framework," *Computer Methods in Applied Mechanics and Engineering*, vol. 278, pp. 524–542, 2014.

[18] L. Xia and P. Breitkopf, "Multiscale structural topology optimization with an approximate constitutive model for local material microstructure," *Computer Methods in Applied Mechanics and Engineering*, vol. 286, pp. 147–167, 2015.

[19] O. Sigmund, "Materials with prescribed constitutive parameters: an inverse homogenization problem," *International J. of Solids and Structures*, vol. 31, no. 17, pp. 2313–2329, 1994.

[20] X. Wang, M. Jiang, Z. Zhou, J. Gou, and D. Hui, "3d printing of polymer matrix composites: A review and prospective," *Composites Part B: Engineering*, vol. 110, pp. 442–458, 2017.

[21] Y. Oosawa, H. Aoki, and H. Yokomizo, "Shaped product of fiber-reinforced composite material and method of manufacturing the same," Mar. 2 2017, US Patent App. 15/247,990.

[22] R. Matsuzaki, M. Ueda, M. Namiki, T.-K. Jeong, H. Asahara, K. Horiguchi, T. Nakamura, A. Todoroki, and Y. Hirano, "Three-dimensional printing of continuous-fiber composites by in-nozzle impregnation," *Scientific reports*, vol. 6, p. 23058, 2016.

[23] N. Li, Y. Li, and S. Liu, "Rapid prototyping of continuous carbon fiber reinforced polylactic acid composites by 3d printing," *J. of Materials Processing Technology*, vol. 238, pp. 218–225, 2016.

[24] W. Payten, B. Ben-Nissan, and D. Mercert, "Optimal topology design using a global self-organisational approach," *International journal of solids and structures*, vol. 35, no. 3-4, pp. 219–237, 1998.

[25] L. Xia, "4 - simultaneous topology optimization of structure and materials," in *Multiscale Structural Topology Optimization*, L. Xia, Ed. Elsevier, 2016, pp. 67 – 88.

[26] T. E. Bruns and D. A. Tortorelli, "Topology optimization of non-linear elastic structures and compliant mechanisms," *Computer methods in applied mechanics and engineering*, vol. 190, no. 26-27, pp. 3443–3459, 2001.

[27] H. A. Eschenauer and N. Olhoff, "Topology optimization of continuum structures: a review," *Applied Mechanics Reviews*, vol. 54, no. 4, pp. 331–390, 2001.

[28] I. Babuška, "Homogenization and its application. mathematical and computational problems," in *Numerical Solution of Partial Differential Equations–III*. Academic Press, 1976, pp. 89–116.

[29] J.-L. Lions, G. Papanicolaou, and A. Bensoussan, *Asymptotic analysis for periodic structures*. Amsterdam: American Mathematical Society, 1978.

[30] D. Cioranescu and J. S. J. Paulin, "Homogenization in open sets with holes," *J. of mathematical analysis and applications*, vol. 71, no. 2, pp. 590–607, 1979.

[31] E. Sanchez-Palencia, "General introduction to asymptotic methods," in *Homogenization Techniques for Composite Media*, E. Sanchez-Palencia and A. Zaoui, Eds. Berlin, Heidelberg: Springer Berlin Heidelberg, 1987, pp. 121–136.

[32] J.-C. Michel, H. Moulinec, and P. Suquet, "Effective properties of composite materials with periodic microstructure: a computational approach," *Computer methods in applied mechanics and engineering*, vol. 172, no. 1-4, pp. 109–143, 1999.

[33] B. Engquist and P. E. Souganidis, "Asymptotic and numerical homogenization," *Acta Numerica*, vol. 17, pp. 147–190, 2008.

[34] P. Kanouté, D. Boso, J. Chaboche, and B. Schrefler, "Multiscale methods for composites: a review," *Archives of Computational Methods in Engineering*, vol. 16, no. 1, pp. 31–75, 2009.

[35] S. J. Hollister and N. Kikuchi, "A comparison of homogenization and standard mechanics analyses for periodic porous composites," *Computational Mechanics*, vol. 10, no. 2, pp. 73–95, 1992.

[36] B. Hassani and E. Hinton, "A review of homogenization and topology optimization ihomogenization theory for media with periodic structure," *Computers & Structures*, vol. 69, no. 6, pp. 707–717, 1998.

[37] L. Xia and P. Breitkopf, "Design of materials using topology optimization and energy-based homogenization approach in matlab," *Structural and multidisciplinary optimization*, vol. 52, no. 6, pp. 1229–1241, 2015.

[38] J. P. Groen and O. Sigmund, "Homogenization-based topology optimization for high-resolution manufacturable microstructures," *International J. for Numerical Methods in Engineering*, vol. 113, no. 8, pp. 1148–1163, 2018.

[39] E. Andreassen and C. S. Andreasen, "How to determine composite material properties using numerical homogenization," *Computational Materials Sci.*, vol. 83, pp. 488–495, 2014.

[40] O. Sigmund and K. Maute, "Topology optimization approaches," *Structural and Multidisciplinary Optimization*, vol. 48, no. 6, pp. 1031–1055, 2013.

[41] O. Sigmund and J. Petersson, "Numerical instabilities in topology optimization: a survey on procedures dealing with checkerboards, mesh-dependencies and local minima," *Structural optimization*, vol. 16, no. 1, pp. 68–75, 1998.

[42] Q. Q. Liang, Y. M. Xie, and G. P. Steven, "Optimal topology selection of continuum structures with displacement constraints," *Computers & Structures*, vol. 77, no. 6, pp. 635–644, 2000.

[43] G. I. Rozvany, "A critical review of established methods of structural topology optimization," *Structural and multidisciplinary optimization*, vol. 37, no. 3, pp. 217–237, 2009.

[44] S. Wang, K. Lim, B. C. Khoo, and M. Y. Wang, "An extended level set method for shape and topology optimization," *J. of Computational Phys.*, vol. 221, no. 1, pp. 395–421, 2007.

[45] N. P. van Dijk, K. Maute, M. Langelaar, and F. Van Keulen, "Level-set methods for structural topology optimization: a review," *Structural and Multidisciplinary Optimization*, vol. 48, no. 3, pp. 437–472, 2013.

[46] L. Blank, H. Garcke, L. Sarbu, T. Srisupattarawanit, V. Styles, and A. Voigt, "Phase-field approaches to structural topology optimization," in *Constrained Optimization and Optimal Control for Partial Differential Equations*, G. Leugering, S. Engell, A. Griewank, M. Hinze, R. Rannacher, V. Schulz, M. Ulbrich, and S. Ulbrich, Eds. Basel: Springer Basel, 2012, pp. 245–256.

[47] J. Kato, D. Yachi, T. Kyoya, and K. Terada, "Micro-macro concurrent topology optimization for nonlinear solids with a decoupling multiscale analysis," *International J. for Numerical Methods in Engineering*, vol. 113, no. 8, pp. 1189–1213, 2018.

[48] E. Andreassen, A. Clausen, M. Schevenels, B. S. Lazarov, and O. Sigmund, "Efficient topology optimization in matlab using 88 lines of code," *Structural and Multidisciplinary Optimization*, vol. 43, no. 1, pp. 1–16, 2011.

[49] R. Rodríguez-Ramos, H. Berger, R. Guinovart-Díaz, J. C. López-Realpozo, M. Würkner, U. Gabbert, and J. Bravo-Castillero, "Two approaches for the evaluation of the effective properties of elastic composite with parallelogram periodic cells," *International J. of Engineering Sci.*, vol. 58, pp. 2–10, 2012.

[50] A. R. Diaz and A. Benard, "Designing materials with prescribed elastic properties using polygonal cells," *International J. for Numerical Methods in Engineering*, vol. 57, no. 3, pp. 301–314, 2003.

[51] J. Robbins, S. Owen, B. Clark, and T. Voth, "An efficient and scalable approach for generating topologically optimized cellular structures for additive manufacturing," *Additive Manufacturing*, vol. 12, pp. 296–304, 2016.

[52] F. Libonati, G. X. Gu, Z. Qin, L. Vergani, and M. J. Buehler, "Bone-inspired materials by design: Toughness amplification observed using 3d printing and testing," *Advanced Engineering Materials*, vol. 18, no. 8, pp. 1354–1363, 2016.

[53] L. Rose, "An application of the inclusion analogy for bonded reinforcements," *International J. of Solids and Structures*, vol. 17, no. 8, pp. 827–838, 1981.

[54] Y.-F. Wu and Y.-Y. Wei, "Effect of cross-sectional aspect ratio on the strength of cfrp-confined rectangular concrete columns," *Engineering Structures*, vol. 32, no. 1, pp. 32–45, 2010.

[55] J. Pereira, E. Fancello, and C. Barcellos, "Topology optimization of continuum structures with material failure constraints," *Structural and Multidisciplinary Optimization*, vol. 26, no. 1-2, pp. 50–66, 2004.